High-Resolution Measurements With a Spaceborne Pencil-Beam Scatterometer Using Combined Range/Doppler Discrimination Techniques

Michael W. Spencer, Wu-Yang Tsai, and David G. Long, *Senior Member, IEEE*

***Abstract*—Conically scanning pencil-beam scatterometer systems, such as the recently launched *SeaWinds* radar, constitute an important class of instruments for spaceborne climate observation. In addition to ocean winds, scatterometer data are being applied to a wide range of land and cryospheric applications. A key issue for future scatterometer missions is improved spatial resolution. Pencil-beam scatterometers to date have been real-aperture systems where only range discrimination is used, resulting in a relatively coarse resolution of approximately 25 km. In this paper, the addition of Doppler discrimination techniques is proposed to meet the need for higher resolution. Here, the unique issues associated with the simultaneous application of range and Doppler processing to a conically scanning radar are addressed, and expressions for the theoretical measurement performance of such a system are derived. Important differences with side-looking imaging radars, which also may employ Doppler techniques, are highlighted. Conceptual design examples based on scatterometer missions of current interest are provided to illustrate this new high-resolution scatterometer approach. It is shown that spatial resolution of pencil-beam scatterometer systems can be improved by an order of magnitude by utilizing combined range/Doppler discrimination techniques, while maintaining the wide-swath and constant incidence angle neaaaaeded for many geophysical measurements.**

***Index Terms*—Ocean winds, radar, backscatter.**

I. Introduction

SEVERAL spaceborne scatterometer missions have been developed and flown in the last decade. These have included the C-band Advanced Microwave Instrument (AMI) on the European Remote Sensing (ERS) satellites, the Ku-band National Aeronautics and Space Administration (NASA) Scatterometer (NSCAT) on the Japanese ADEOS-I mission, as well as the more recent Ku-band NASA *SeaWinds* instrument on the QuikSCAT spacecraft [2], [19], [29]. A scatterometer obtains winds over the ocean by measuring the surface backscatter cross section at several different azimuth angles. Scatterometer-derived ocean surface wind measurements have contributed significantly to the scientific study of air/sea interactions and global climate phenomena such as El Niño, and scatterometer winds are being increasingly used to improve the fidelity of numerical weather forecasts [1], [4], [12].

In addition to ocean winds, scatterometer backscatter data are being applied to an expanding list of land and ice applications. Scatterometer data have proven valuable in these research areas because of superior earth coverage compared with other active microwave instruments (*SeaWinds*, for example, achieves near global coverage daily), as well as excellent radiometric stability that enables the detection of subtle climate change signatures [17], [35], [36]. Examples of emerging applications include polar ice mapping [13], [17], [24], [25], snow coverage and depth analysis [20], [35], soil freeze/thaw tracking [26], vegetation classification and change studies [11], [16], [27], and soil moisture retrieval [34]. Scatterometer data are also useful when combined in a supplementary fashion with radiometer data for sea ice classification and ocean salinity retrieval [21], [25]. Motivated by the successful use of scatterometer data in both wind and nonwind applications, a variety of future scatterometer missions are being planned [14], [21], [30].

To date, two different scatterometer system implementations have been flown: the *fan-beam* approach, which employs multiple, fixed-position antennas with broad beams to form the measurement swath, and the *pencil-beam* approach, where a single narrow-beam antenna is conically rotated about the nadir axis to form the measurement swath [28]. The fan-beam approach has been utilized extensively, beginning with the Seasat-A scatterometer (SASS) and continuing with the NSCAT and ERS systems. In the present analysis, however, our focus shall be on the increasingly important pencil-beam approach, which was selected for the *SeaWinds* series of instruments. The following are key features of the pencil-beam approach that make it advantageous in many cases.

1) A single rotating antenna is often more easily accommodated on spacecraft than multiple fixed antennas.
2) The conical scanning geometry allows a wide swath of measurements to be obtained at a constant incidence angle, which is desirable for many geophysical applications.
3) Multiple polarizations and/or simultaneous radiometer measurements are more easily accomplished with this antenna design [10], [29], [32].

Although only Ku-band systems have flown to date, pencil-beam systems employing other frequencies, such as L-band have, been proposed [21].

Manuscript received July 9, 2001; revised October 3, 2002. This work was performed by the Jet Propulsion Laboratory, California Institute of Technology, under contract with the National Aeronautics and Space Administration.

M. W. Spencer and W.-Y. Tsai are with the Jet Propulsion Laboratory, California Institute of Technology, Pasadena, CA 91109-8099 USA (e-mail: Michael.W.Spencer@jpl.nasa.gov).

D. G. Long is with Brigham Young University, Microwave Earth Remote Sensing Laboratory, Department of Electrical and Computer Engineering, Provo, UT 84602 USA (long@ee.byu.edu).

Digital Object Identifier 10.1109/TGRS.2003.809938

A key challenge for the design of future pencil-beam scatterometers is the improvement of spatial resolution. Current pencil-beam instruments are real-aperture systems—where range discrimination is employed, but the resolution is nevertheless limited by the antenna beamwidth [29]. The *SeaWinds* scatterometer has a beamwidth-limited resolution of approximately 25 km, which is too coarse for many geophysical applications. An order-of-magnitude improvement in resolution is required to observe many mesoscale wind features associated with storms and in coastal waters [9], [23]. For land and ice applications, spatial resolution comparable with visible/IR imaging radiometers—such as the 1–5-km resolution Advanced Very High Resolution Radiometer (AVHRR)—is desired [3], [26], [31].

With current scatterometer systems, resolution limitations have been partially overcome by the application of various resolution enhancement algorithms applied as a postprocessing step [6], [15], [17], [22], [29]. With these techniques, multiple, overlapping backscatter measurements are used to solve for the underlying scene at higher resolution than that obtained with the beamwidth-limited instantaneous footprint. Because these techniques involve multiple observations of the same point on the surface, either from multiple azimuth directions or multiple orbit passes, they are termed "multipass" techniques. A significant limitation of multipass techniques is that the target scene must be assumed temporally stable and/or azimuthally isotropic. These assumptions are invalid for ocean wind measurements and are problematic for quickly varying land and ice events. It is, therefore, desirable to achieve high resolution with more conventional "single-pass" means—i.e., by reducing the instantaneous dimensions of the measurement cell or pixel.

An established method for improving resolution beyond the real-aperture limit is to employ Doppler discrimination along with range discrimination in order to further sharpen the spatial dimensions of the measurement cell. This approach is the basis of synthetic aperture radar (SAR)—widely used in high-resolution imaging applications—but has not been previously applied to the conically scanning scatterometer case. In this paper, combined range/Doppler discrimination techniques are proposed as a means to improve the single-pass resolution of future pencil-beam scatterometer systems. The unique considerations associated with the addition of Doppler discrimination to a conically scanning radar are described, and expressions for the fundamental performance constraints and best theoretical resolution of such a system are derived. To illustrate the utility of the combined range/Doppler resolution approach, two conceptual design examples based on pencil-beam scatterometer systems of current interest are provided. It is shown that an order-of-magnitude improvement in spatial resolution can be achieved by adding Doppler discrimination, albeit with requirements for a somewhat larger antenna and increased pulse repetition frequency (PRF) relative to real aperture systems. Finally, as an additional tool for more detailed design analyses, a generalized equation for the point target response associated with a conically scanning scatterometer system is derived. This equation is shown to validate the simplified design equations presented in the preceding sections. Taken as a whole, this study is intended to form a conceptual design framework for future high-resolution pencil-beam systems.

II. Pencil-Beam Scatterometer Concepts and Definitions

In this section, key definitions and concepts referred to throughout this paper are discussed. The measurement geometry for a conically scanning radar is illustrated in Fig. 1(a). From a height h above the earth, the antenna beam is conically scanned about the nadir axis. The antenna boresight maintains a constant incidence angle $\theta_{\rm inc}$ with the surface. The boresight line intersects the surface at a slant range R from the satellite, and at a distance d as measured along the earth from the nadir point. The continuously rotating antenna thus forms a total measurement swath of width $2d$. (Note that the computation of these parameters must take the significant earth curvature effect into account.) The antenna spins at an angular rate Ω, where the instantaneous scan position of the antenna beam is given by the azimuth angle $\theta_{\rm az}$. The spacecraft orbital speed is given by $v_{\rm sc}$, and the effective ground speed of the subsatellite point is given by v_g. The specific spacecraft orbital elements and the measurement geometry are selected to yield the desired earth coverage, with an incidence angle appropriate for the geophysical parameters of interest.

For resolution analysis, it is convenient to define a set of coordinates which are locally fixed with respect to the antenna footprint as it is scanned over the surface. The *azimuth* axis is defined to be in the local direction of footprint movement due to the rotation of the antenna [see Fig. 1(b) and (c)]. The azimuth axis is parallel to the direction of spacecraft motion when $\theta_{\rm az} = 90^\circ$ or 270°. Perpendicular to the azimuth axis is the *elevation* axis, which is in the direction of increasing range along the surface. The azimuth and elevation dimensions of the antenna footprint are given by $x_{\rm az}$ and $x_{\rm el}$, respectively. For a pencil-beam system, it is generally true that $x_{\rm el} \ll d$, insuring that only a narrow range of incidence angles is covered by the footprint.

For many radar applications spatial resolution better than that delimited by the antenna footprint dimensions is desired. Fig. 1(b) and (c) illustrates two primary techniques for obtaining subfootprint resolution with a pencil-beam scatterometer system. The real-aperture approach, where only range discrimination is employed, is diagramed in Fig. 1(b). The *resolution cell* is indicated by the shaded region. Here, the azimuth resolution is the azimuthal width of the antenna footprint $x_{\rm az}$. The elevation resolution $\delta_{\rm el}$ is achieved by applying range processing to the radar echo return, forming narrow elevation "slices" through the footprint. The real-aperture approach is relatively easy to implement in hardware and is employed with *SeaWinds* [29]. The key disadvantage of this approach is that large antenna apertures are required to obtain the finest desired resolution. For example, to achieve 1-km azimuth resolution with a Ku-band system operating with the same measurement geometry as *SeaWinds* an antenna length over 20 m would be required.

In order to obtain improved azimuth resolution without resorting to an unrealistically large rotating antenna, the target scene can be discriminated in both range and Doppler simultaneously. The resulting resolution for a pencil-beam system is shown conceptually in Fig. 1(c). In this case, the azimuth width of the resolution cell $\delta_{\rm az}$ is determined by the Doppler

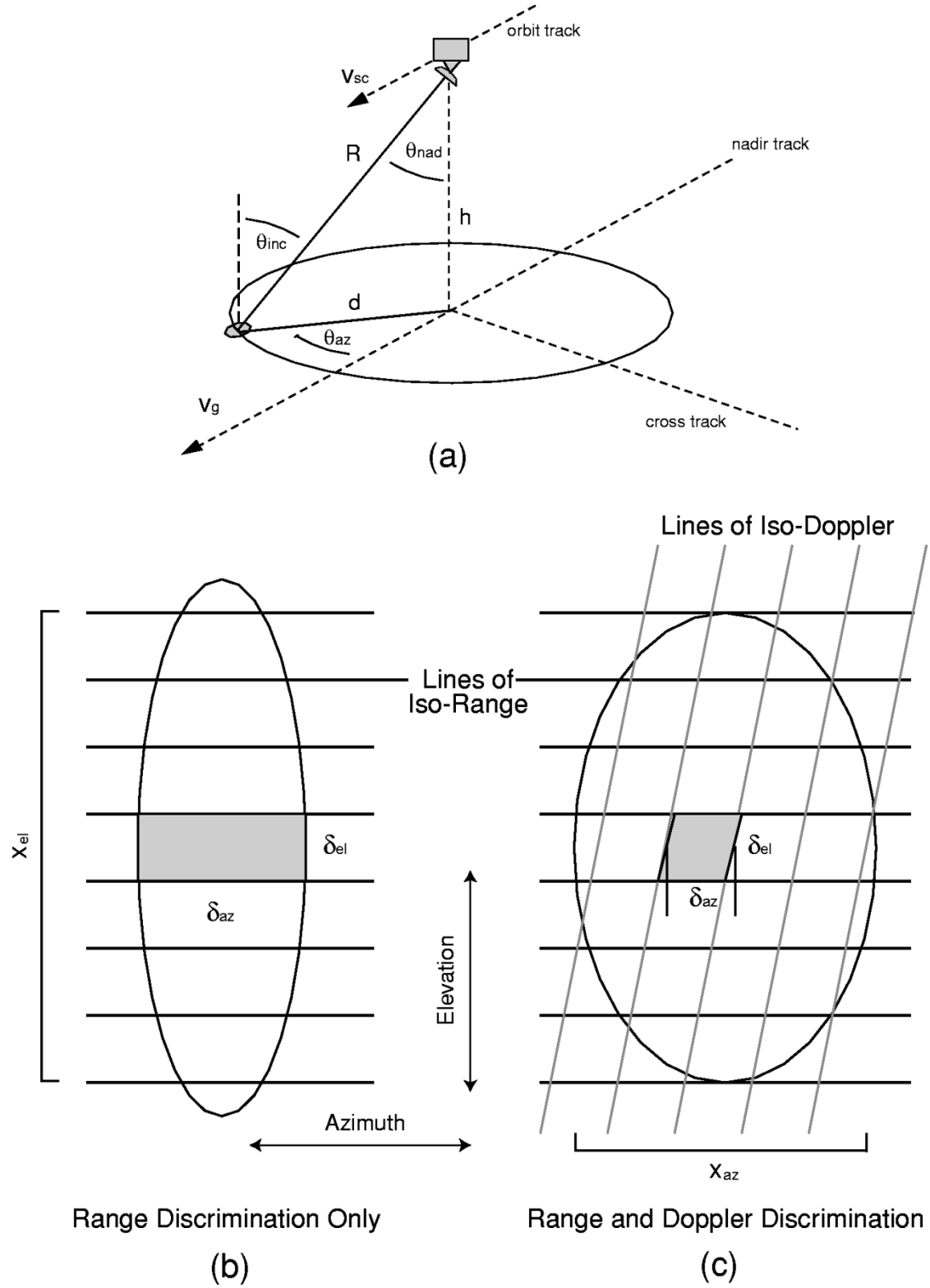

Fig. 1. (a) Overall conically scanned pencil-beam scatterometer geometry. (b) Conceptual illustration of range-only resolution approach. (c) Conceptual illustration of combined range and Doppler resolution approach. The oval is a representation of the antenna two-way 3-dB footprint projected on the surface. In both (b) and (c), the resolution cell is denoted by the shaded region, and the spacing between the iso-range and iso-Doppler lines represent the range and Doppler resolution inherent to the instrument design and processing.

resolution achieved by the instrument and processor design. Combined range/Doppler processing can be viewed as a correlation operation applied to an echo pulse train which extracts the backscattered energy from specific locations (or trajectories) in range/Doppler space [33]. Key design considerations include the selection of an antenna pattern and PRF which minimize range and Doppler ambiguities, and which yield the desired azimuth resolution and swath width. Such techniques

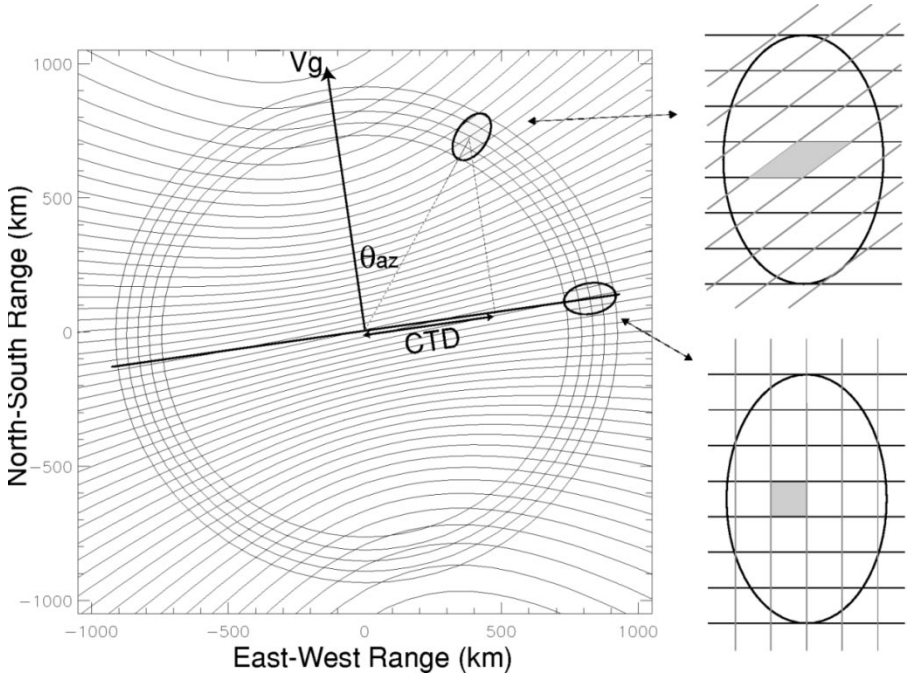

Fig. 2. Lines of iso-Doppler and iso-range for 800-km sun-synchronous orbit at ascending equator crossing. The hyperbolic iso-Doppler contour spacing is 20 kHz. Also shown are circles representing the iso-range contours associated with the antenna footprint. Other iso-range lines, if plotted, would appear as more concentric circles likewise centered on the nadir point. The sidebar at right illustrates the relationship of the range/Doppler contours local to the antenna footprint for two antenna azimuth positions, with the shaded region representing the resolution cell.

are the foundation of SAR, which has been used extensively for high-resolution imaging applications, and form the basis for the improved-resolution scatterometry discussed in the present analysis.

Although the application of Doppler techniques to a conically scanning scatterometer system is similar in principle to the familiar SAR case, there are key differences. SAR systems typically employ array antennas which view the surface at a fixed (usually side-looking) azimuth angle—as in strip-map or scan-SAR—or are steered in azimuth to dwell on a specific target region—as in spotlight-SAR. In order to obtain multiple azimuth angle measurements over a wide swath, however, the antenna footprint of a pencil-beam scatterometer is continuously rotated away from the target scene at a rate much faster than that generated by the spacecraft motion alone. This dramatically reduces the target dwell time relative to conventional SAR and thus limits the achievable azimuth resolution. Another consideration for a conically scanned radar is that the azimuth angle of the measurements varies over the measurement swath. This is equivalent to having a different squint angle for each measurement, and leads to a variation in resolution performance over the swath. In order to address these and other considerations in detail, a new design framework is needed that adapts established Doppler techniques to the unique issues associated with a conically scanned radar geometry.

III. Instrument Design Considerations for Pencil-Beam Scatterometers Employing Simultaneous Range/Doppler Discrimination

In this section, key considerations governing the design and performance of a conically scanned scatterometer utilizing combined range/Doppler discrimination techniques are addressed. Familiarity with current scatterometer and radar remote sensing techniques is assumed, and emphasis is therefore on the unique system design issues posed by such an approach. This analysis results in a set of equations that can be used for conceptual design tradeoffs in the development of future high-resolution pencil-beam scatterometer systems.

A. Doppler Geometry and Azimuthal-Dependent Resolution Effects

When applying Doppler discrimination techniques, a fundamental consideration is the geometrical relationship of the range and Doppler contours over the entire region scanned by the antenna. In Fig. 2, contours of iso-range and iso-Doppler are plotted for the example case of an 800-km sun-synchronous orbit (the same as *SeaWinds* [29]). The antenna beam position is termed "side-looking" when $\theta_{\rm az} = 90^\circ$ or 270°, and "forward-" or "aft-looking" when $\theta_{\rm az} = 0^\circ$ or 180°, respectively. Note that the pencil-beam azimuth angle $\theta_{\rm az}$ is the complement of the squint angle as typically defined for SAR systems. The cross-track distance (CTD) is defined to be the distance of a given measurement from the spacecraft nadir track.

The above described Doppler geometry has important implications for the azimuth resolution over the swath. For the short footprint dwell times achievable with a scanning pencil-beam system (see Sections III-D and III-G), a spatial resolution cell may be modeled as delimited by the intersection of range and Doppler bands, where the width of these bands corresponds to the Doppler and range resolution achieved by the radar instrument. When the antenna is pointed to the side-looking direction, the angle between the Doppler and range contours in the vicinity of the footprint is 90°, and the resolution cell is rectangular. As the antenna is scanned (or squinted) toward the forward or aft direction, however, we observe from Fig. 2

that the Doppler contours shift from perpendicular to parallel with the range contours. This rotation of the iso-Doppler lines distorts the resolution cells into a parallelograms whose azimuth width $\delta_{\rm az}$ is elongated with respect to the azimuth width for the side-looking geometry [33]. This elongation effect is further enhanced by the fact that the spacing between the iso-Doppler lines on the surface grows wider as the antenna is rotated away from the side-looking direction (again, see Fig. 2). We shall term the total azimuth resolution degradation relative to that for side-looking pointing "squint elongation."

An exact quantification of squint elongation requires a calculation that includes accurate satellite orbit propagation, earth rotation, and earth oblateness effects (these are taken into account in producing the iso-Doppler contours of Fig. 2). The assumption of a nonrotating spherical earth, however, yields results with sufficient accuracy for the concept analysis presented here. Adopting this assumption, the first derivatives of the Doppler shift components along the elevation and azimuth directions in the vicinity of the surface footprint $s'_{\rm el}$ and $s'_{\rm az}$ are approximated by

$$\begin{aligned} s'_{\rm az} &= [-2v_{\rm sc}\sin(\theta_{\rm az})]/[R\lambda] \\ s'_{\rm el} &= [2v_{\rm sc}\cos(\theta_{\rm az})(1-\sin^2(\theta_{\rm inc}))]/[R\lambda]. \end{aligned} \tag{1}$$

Because the iso-range lines are locally parallel to the footprint azimuth axis, the angle between the iso-Doppler and iso-range contours ψ is

$$\psi = \arctan\left(\frac{s'_{\rm el}}{s'_{\rm az}}\right) \tag{2}$$

and the magnitude of the Doppler frequency gradient along the surface of the earth s' is given by

$$s' = \sqrt{(s'_{\rm el})^2 + (s'_{\rm az})^2}. \tag{3}$$

Using these definitions, the "angular" component of the elongation, $f_{\rm ang}(\theta_{\rm az})$, due to the rotation of the iso-Doppler lines is

$$f_{\rm ang}(\theta_{\rm az}) = \frac{1}{\cos\psi} \tag{4}$$

and the additional elongation due the Doppler contour spacing $f_{\rm sp}(\theta_{\rm az})$ is

$$f_{\rm sp}(\theta_{\rm az}) = \frac{s'(\theta_{\rm az})}{s'(\theta_{\rm az}=90^\circ)}. \tag{5}$$

In Fig. 3, the angular and Doppler spacing elongation effects, as well as the combined elongation effect given by $f(\theta_{\rm az}) = f_{\rm ang}(\theta_{\rm az})f_{\rm sp}(\theta_{\rm az})$, are plotted versus CTD for the geometry corresponding to Fig. 2. (Similar curves apply for other orbit and scan geometries.) The significance of Fig. 3 for the present analysis is that, unlike the conventional real-aperture case where azimuth resolution is essentially a constant value over the measurement swath, the azimuth resolution for the pencil-beam scatterometer case is highly dependent on cross-track position. As an illustration, consider that a system design capable of achieving 1-km azimuth resolution at a cross-track distance of 800 km (side-looking case) can only obtain an azimuth resolution of 2 km at a cross-track distance of 400 km, and 4 km at 200-km cross-track. The azimuth resolution quickly degrades near the nadir track, ultimately becoming the same as that achieved by a real-aperture system. The variation in azimuth resolution over the swath must be taken into account when assessing the performance of a high-resolution pencil-beam design.

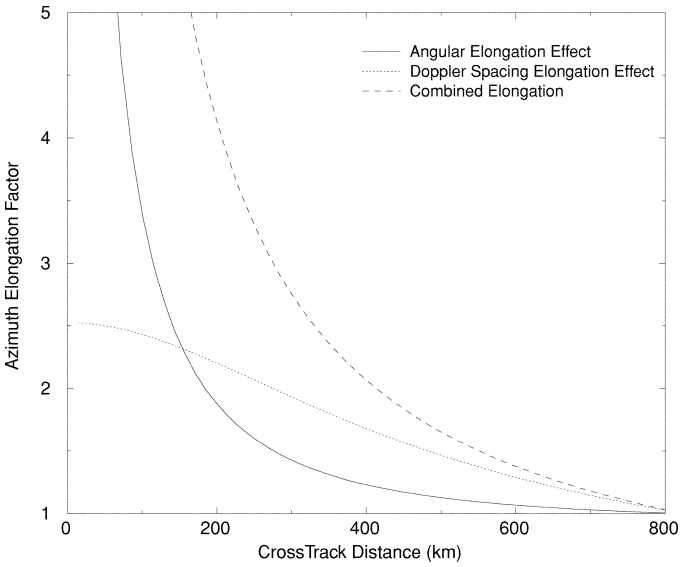

Fig. 3. Angular, Doppler spacing, and combined elongation effect for scan geometry of Fig. 2.

B. Range/Doppler Ambiguity Considerations

Another fundamental consideration is the suppression of range and Doppler ambiguities associated with the transmitted waveform [5]. Ambiguity rejection constraints limit the allowable dimensions of the antenna footprint, and hence strongly impact the overall resolution performance of the radar design. The ambiguity issue can be visualized and addressed in a variety of ways. Given the rapid scanning motion of the antenna, an analysis based on the radar ambiguity function is found to be particularly useful for the pencil-beam scatterometer case. Our approach here is to first perform an ambiguity function analysis for the side-looking geometry and then extend these results to the case of arbitrary azimuth angle.

In Fig. 4, a conceptual depiction of the ambiguity function of a periodic pulse train is shown (see [33]). The dark spots represent the location of ambiguities in delay/Doppler space—the center spot representing the location of the desired resolution cell. For the short footprint dwell times associated with a scanning pencil-beam system (see Sections III-D and III-G), the desired resolution cell is approximated as fixed in range/Doppler space for this analysis. The other spots represent locations of unwanted ambiguities spaced at multiples of PRF and the pulse repetition interval (PRI = 1/PRF) along the Doppler and delay axes, respectively. As illustrated by Fig. 2, the local delay/Doppler coordinates may be transformed into elevation/azimuth coordinates, where the transformation is a function of the antenna azimuth position $\theta_{\rm az}$. For the side-looking case, the delay/Doppler axes are parallel to the elevation/azimuth axes (illustrated in Fig. 4).

In order to unambiguously detect the echo at the desired resolution cell, the unwanted ambiguity peaks must be suppressed by appropriate design of the antenna gain pattern. In Fig. 4,

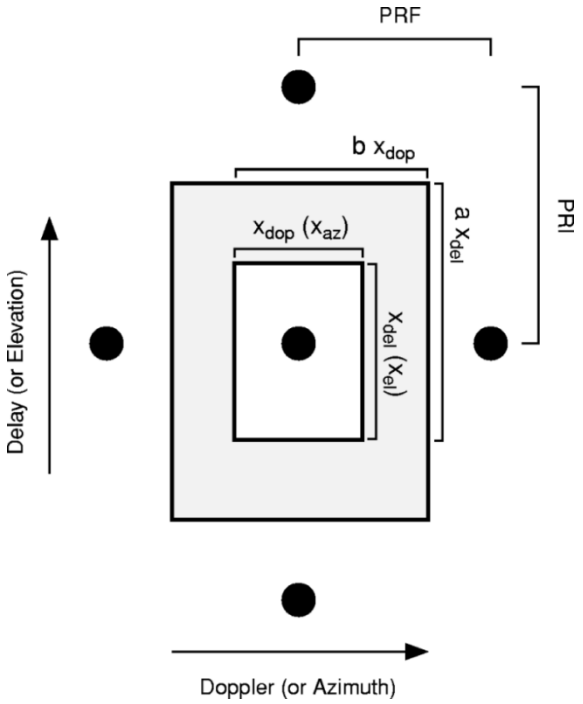

Fig. 4. Spatial ambiguity diagram for the side-looking geometry. Dark spots represent Doppler/delay ambiguities for side-looking case. Concentric squares represent antenna pattern, with the center region defined as the usable footprint area.

the effect of the antenna pattern is conceptually illustrated by concentric rectangles which represent contours of the two-way antenna gain pattern as projected on the delay/Doppler plane (or, equivalently for the side-looking case, on the elevation/azimuth plane). The outer rectangle is a suitable "buffer" region that produces the desired level of ambiguity suppression. This contour may correspond, for example, to the -20-dB point in the two-way antenna pattern. The inner rectangle represents the "usable" region of the antenna footprint within which individual scatterers can be unambiguously detected. This contour, for instance, could correspond to the -3-dB level of the antenna pattern. The dimensions of the usable footprint in delay/Doppler space are $x_{\rm del}$ and $x_{\rm dop}$ and are related to the dimensions of the outer contour by the parameters a and b as shown in Fig. 4. For the side-looking case, these dimensions are approximately related to the equivalent elevation/azimuth dimensions by

$$x_{\rm el} = \frac{c}{2\sin\theta_{\rm inc}}\, x_{\rm del} \tag{6}$$

and utilizing (1) with $\theta_{\rm az} = 90^\circ$

$$x_{\rm az} = \frac{R\lambda}{2v_{\rm sc}}\, x_{\rm dop}. \tag{7}$$

As discussed later, the best azimuth resolution is achieved by *maximizing* the usable footprint size. The relationship between the usable footprint dimensions in delay/Doppler space and the PRF is summarized by

$$ax_{\rm del} \le \text{PRI} \quad bx_{\rm dop} \le \text{PRF}. \tag{8}$$

Recalling that $\text{PRF} = 1/\text{PRI}$, we combine the two inequalities in (8) to write

$$x_{\rm del}x_{\rm dop} \le \frac{1}{ab}. \tag{9}$$

Using (8) and (9), we can then write

$$x_{\rm el}x_{\rm az} \le \frac{cR\lambda}{4abv_{\rm sc}\sin\theta_{\rm inc}}. \tag{10}$$

Equation (10) is a key result for the current analysis. Based on ambiguity suppression considerations, it establishes a maximum constraint on the usable footprint dimensions.

Strictly speaking, (10) is valid only for the side-looking geometry. As the antenna is scanned forward or backward of this position, the Doppler and azimuth axes are no longer parallel as shown in Fig. 4, but are rotated and transformed consistent with (1)–(5). As viewed from the perspective of the elevation/azimuth plane, this transformation neither changes the shape nor dimensions of the projected antenna footprint (which is still $x_{\rm el} \times x_{\rm az}$), or the location of the ambiguities on the elevation axis. However, the loci of the ambiguities along the azimuth axis change, with the azimuth spacing between the ambiguities growing larger due to the same geometrical effects that lead to squint elongation discussed in Section III-A. Consequently, as the antenna position points forward or aft, there is generally less contamination from the azimuth ambiguities than for the side-looking geometry. Equation (10) thus represents the limiting case, and we conclude that if the ambiguity constraint is satisfied for the side-looking case, it is satisfied at all other scan positions as well for pencil-beam systems we consider. (This argument is validated in a more quantitative fashion in Section V.)

An important application of the constraint provided by (10) is the specification of antenna design parameters. In order to illustrate the tradeoffs associated with the antenna beamwidth, usable footprint dimensions, ambiguity level, and the a and b parameters, the design curves in Fig. 5 have been constructed. Here, the maximum ambiguity level associated with scatterers within the usable footprint is plotted versus a (if elevation/range ambiguities are being addressed) or b (if azimuth/Doppler ambiguities are being addressed). Each curve, in turn, represents a different value of the usable footprint width expressed as a fraction of the two-way 3-dB beamwidth. The parameter χ is defined as $\chi_{\rm el} = x_{\rm el}\cos\theta_{\rm inc}/R\beta_{\rm el}$ for the elevation dimension, and $\chi_{\rm az} = x_{\rm az}/R\beta_{\rm az}$ for the azimuth dimension. The ambiguity levels are computed assuming a representative antenna gain pattern rolloff function (Bessel function squared, in this case). As an example of the application of this plot, if the requirement for ambiguities is -20 dB and the usable footprint is defined by the two-way 3-dB antenna contour, then $\chi_{\rm el} = \chi_{\rm az} = 1$, and from Fig. 5, $a = b = 1.72$.

Inserting the definitions for $\chi_{\rm el}$ and $\chi_{\rm az}$ into (10)

$$\beta_{\rm el}\beta_{\rm az} \le \frac{c\lambda\cot\theta_{\rm inc}}{4ab\chi_{\rm el}\chi_{\rm az}Rv_{\rm sc}}. \tag{11}$$

Equation (11) represents a constraint on the product of the antenna beamwidths and consequently on the minimum antenna area and is similar to constraints used in the design of conventional SAR systems [5]. It is important to note that depending on the requirements for a given application, an antenna with larger

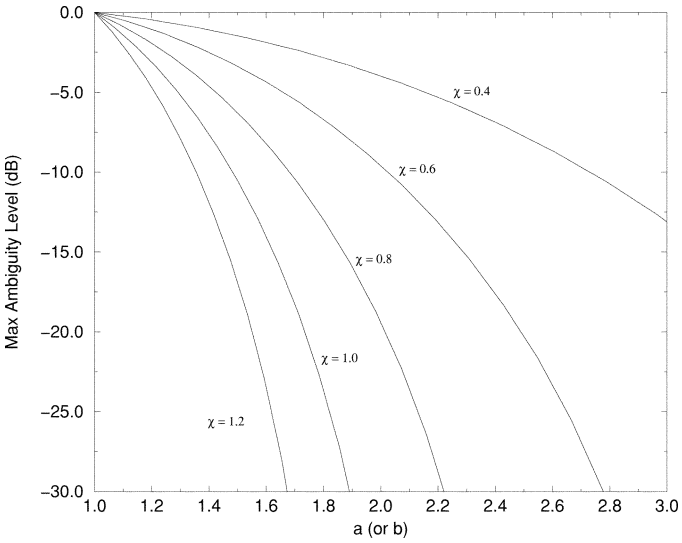

Fig. 5. Design curves for trading off antenna beamwidth, ambiguity, and the a and b parameters (see text).

beamwidth (and hence smaller effective area) may be acceptable if either the ambiguity suppression requirement is relaxed or if a smaller footprint can be tolerated [8].

C. Antenna Spin Rate Considerations

Closely related to the antenna footprint dimensions is the selection of the antenna rotation rate. As will be demonstrated in the next section, the rotation rate is a key factor in determining the azimuth resolution when Doppler techniques are applied to a conically scanning scatterometer. Here, we discuss the constraints and considerations that apply to the selection of the antenna rotation rate.

Along-Track Continuity Constraint: The primary factor which determines the antenna rotation rate is the "along-track continuity constraint." In order to achieve complete surface coverage over the swath, the measurements from consecutive rotations of the antenna must be contiguous. To ensure this, the distance the spacecraft ground trace moves during one rotation of the antenna must be no larger than the elevation width of the footprint, $x_{\rm el}$. This constraint is summarized by

$$\Omega \geq \frac{v_g}{x_{\rm el}} \tag{12}$$

where Ω and v_g are the rotation rate and ground velocity of the spacecraft as defined in Section II.

A consequence of (12) is that smaller antenna footprints require faster antenna rotation rates to obtain complete surface coverage. In general, however, the higher angular momentum that results from faster spin rates is undesirable because it requires a larger and more complex spacecraft attitude control system. In situations where it is undesirable to lengthen $x_{\rm el}$—such as when range ambiguities must be rejected—multiple antenna beams offset in elevation so as to cover a wider elevation range must be used [21]. When this approach is adopted, (12) becomes

$$\Omega \geq \frac{v_g}{N_b x_{\rm el}} \tag{13}$$

where N_b is the number of independent elevation beams employed. The term "independent" here means that the beams are sufficiently isolated in space, frequency, or polarization so that ambiguities associated with one beam do not contaminate the adjacent beams.

Scanning Loss: In addition to surface coverage and angular momentum considerations, another factor in the selection of antenna spin rate is "scanning loss." During the round-trip flight time of the radar pulse to the surface and back, the antenna beam is rotated to point in a different direction than at the time of transmit. Scanning loss is defined as the loss of signal power that occurs because of this antenna pattern offset [18], [28]. This loss lowers the SNR and, as discussed in Section III-E, impacts the measurement accuracy. Assuming that the slant range R is approximately constant over the footprint, the scanning loss $L_{\rm scan}$ is defined by

$$L_{\rm scan} = \frac{\int g_{\rm tx}(\overline{r}) g_{\rm rx}(\overline{r})\, dA}{\int g_{\rm tx}^2(\overline{r})\, dA} \tag{14}$$

where $\vec{r}$ is the loci of a point on the surface. Here, $g_{\rm tx}(\overline{r})$, and $g_{\rm rx}(\overline{r})$ are the beam patterns on the surface at the time of transmit and receive, respectively; the integral is performed over the illuminated surface region. When $x_{\rm el} \ll d$, the antenna pattern motion during the pulse flight time can be modeled as a simple translation in the azimuth direction $\Delta x_{\rm scan}$ where

$$\Delta x_{\rm scan} = \frac{2R\gamma}{c} \tag{15}$$

and the parameter γ is defined to be the translational speed of the footprint in the azimuth direction due to the scanning motion given by

$$\gamma = 2\pi\, d\Omega. \tag{16}$$

Using (14) and (15), the scanning loss is plotted as a function of the separation factor, ρ, in Fig. 6. Here, ρ is defined as the azimuth displacement normalized by the two-way azimuth beamwidth (i.e., $\rho = \Delta x_{\rm scan}/R\beta_{\rm az}$). As expected, the scanning loss increases with increasing azimuth displacement. The allowable signal loss is dependent on the measurement accuracy requirements for the specific system design.

Thus far, we have only considered the case where the same antenna beam is used for both transmit and receive. If the scanning loss according to Fig. 6 is excessive, the application of azimuthal beam steering may be required. The antenna beam is steered, in effect, to different positions in azimuth alternately on transmit and receive so as to compensate for the azimuth separation given by (15). Transmit/receive azimuth steering may be accomplished, for example, by using two adjacent feeds—one which looks slightly ahead in azimuth and one slightly behind. In general, such azimuth steering complicates the antenna design and calibration, so it is desirable to use a single beam where possible (as is the case for *SeaWinds*). Combining the along-track continuity constraint in (13) with the scanning-loss considerations, a constraint on the antenna beam dimensions such that a single beam may be used for both transmit and receive is given by

$$\beta_{\rm el}\beta_{\rm az} \geq \frac{4\pi d v_g \cos\theta_{\rm inc}}{c N_b R \rho_{\rm min}} \tag{17}$$

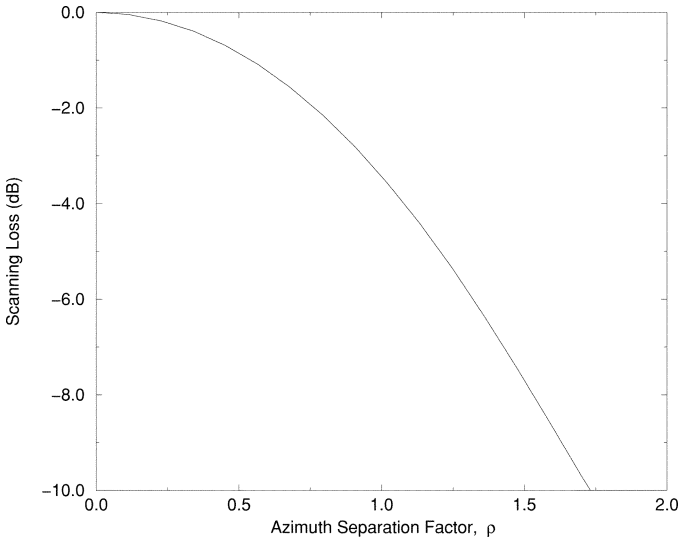

Fig. 6. Example of scanning loss (in decibels) versus scan separation factor ρ. For the purposes of analysis, the antenna pattern has been modeled as a uniformly illuminated circular aperture. Due to the normalization by the antenna beamwidth in calculating ρ, however, sensitivity to the precise antenna illumination for the calculated scanning loss is small.

where $\rho_{\min}$ is the separation factor that corresponds to the maximum acceptable scanning loss for a given application. Equation (17) indicates that narrower beam antennas are more likely to require the additional complexity of transmit/receive beam steering.

D. Spatial Resolution

With constraints established for the usable footprint dimensions and antenna spin rate, we return to the topic of spatial resolution. When range discrimination is employed, the finest elevation resolution achieved $\delta_{\rm el}$ is

$$\delta_{\rm el} = \frac{c}{2\sin\theta_{\rm inc} B_t} \tag{18}$$

where B_t is the bandwidth of the transmit pulses. Note that (18) applies to all remote sensing radars, including real-aperture scatterometer systems and SAR. The key point of departure in the analysis of high-resolution conically scanning scatterometers is the calculation of azimuth resolution. Due to the rapid scanning motion, commonly used design equations developed for conventional SAR systems do not fully apply.

The fundamental limit on azimuth resolution is determined by the antenna dwell time—i.e., the length of time a given scatterer is observed as the antenna footprint sweeps past. The relationship between the Doppler resolution $\delta_{\rm dop}$ and the dwell time τ_d is approximately $\delta_{\rm dop} = 1/\tau_d$. Employing an approximation similar to that used to obtain (7), the achievable azimuth resolution $\delta_{\rm az}$ is

$$\delta_{\rm az} = \frac{R\lambda}{2v_{\rm sc}\tau_d} f(\theta_{\rm az}). \tag{19}$$

Here, the first (quotient) term is the azimuth resolution for the side-looking geometry, and the term $f(\theta_{\rm az})$ represents the degradation in resolution due to squint elongation effects as discussed in Section III-A.

The maximum available footprint dwell time for a given point on the surface is

$$\tau_d = \frac{x_{\rm az}}{\gamma} \tag{20}$$

where $x_{\rm az}$ is the azimuthal width of the usable footprint, and γ is the azimuthal ground speed of the footprint due to the scanning motion as defined (16). Note that because γ is typically much greater than v_g, the dwell time available is dramatically shorter for the scanning pencil-beam case when compared to the typical SAR case. The shorter dwell time reduces the azimuth resolution and is the price paid for the extremely wide swath achieved by the conically scanned pencil-beam approach.

Inserting (20) into (19), applying both the along-track continuity constraint of (15) and the maximum usable footprint constraint in (10), and making the conservative assumption that $v_g \approx v_{\rm sc}$; the best achievable azimuth resolution is then

$$\delta_{\rm az} \geq \frac{4\pi d v_{\rm sc}\sin\theta_{\rm inc} ab}{N_b c} f(\theta_{\rm az}). \tag{21}$$

Equation (21) indicates that $\delta_{\rm az}$ is not a direct function of antenna size or carrier frequency, but depends only on the orbit and measurement geometry, the required ambiguity level (via a and b), and the number of independent elevation beams. The example system designs presented in Section IV demonstrate that a value of $\delta_{\rm az}$ on the order of 1 km can be readily achieved using this approach. This is significantly finer resolution than can realistically be achieved with real-aperture systems, but coarser than that achieved by typical SAR systems.

E. Transmit Pulse Timing

A practical consideration to be addressed in the design process is the selection of a radar timing scheme that ensures that the transmission of pulses does not interfere with the reception of echo returns. In the development of (21), it was assumed that a given scatterer is observed for the entire footprint dwell time—i.e., that the radar is pulsing continuously. This continuous pulse timing scheme is illustrated in Fig. 7(a). In addition to meeting the constraints in (8), the PRI must be selected to allow proper interleaving of the transmit events and receive echos. Quantitatively this interleaving constraint can be expressed as

$$\left|\left(n-\frac{1}{2}\right)\mathrm{PRI} - \frac{2R}{c}\right| \leq \frac{\mathrm{PRI} - 2T_p - x_{\rm del} - \Delta T_{\rm marg}}{2} \tag{22}$$

where n is an integer representing the number of pulses in flight; T_p is the pulse length; $x_{\rm del}$ is the round-trip delay between the inner and outer edges of the usable footprint [see (6)]; and $\Delta T_{\rm marg}$ is timing margin allowed for uncertainties in the precise value of R. A corollary to (22) is a limit on the transmit pulse length that is given by

$$T_p \leq \frac{\mathrm{PRI} - x_{\rm del} - \Delta T_{\rm marg}}{2}. \tag{23}$$

For the wide-swath and high-incidence angles typically used for pencil-beam scatterometers, however, the constraints of (8) and (22) may be difficult to meet. This is particularly true if significant timing margins are required in order to allow for spacecraft attitude variations and for land surface topography. We also

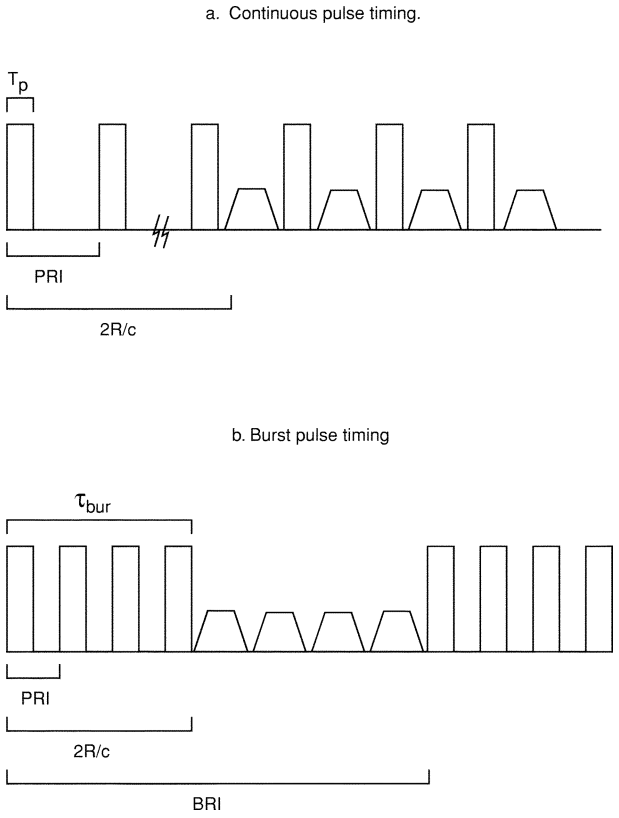

Fig. 7. Pulse timing schemes. (a) Continuous. (b) Burst. Rectangles represent transmit events, and trapezoids represent return echoes.

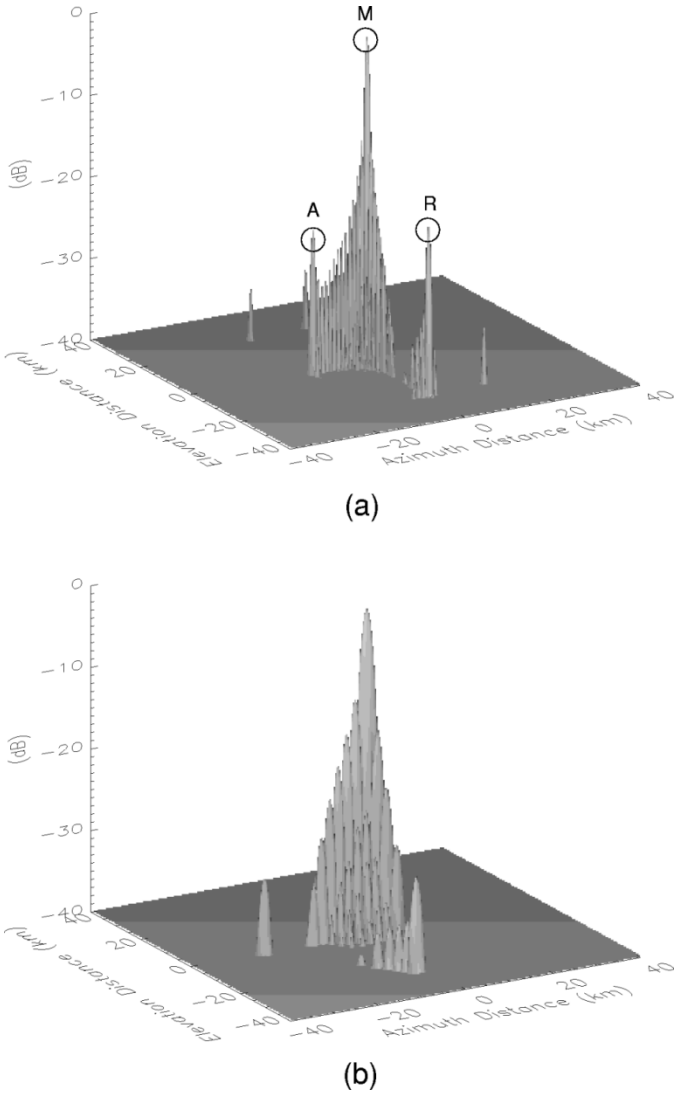

Fig. 8. Sample PTRF diagram. (a) For side-looking geometry. The main ambiguity is indicated by "M," the first azimuth ambiguity by "A," and the first range ambiguity by "R." The side-looking response function for $\theta_{\rm az} = 30^\circ$ is shown in (b) (exactly side-looking) for center pixel.

see from (23) that, after the beam filling effect and necessary timing margin are taken into account, the available time for the transmit pulse width is limited. One solution to these problems is to adopt a burst pulsing scheme as shown in Fig. 8(b). For this timing scheme, a multiple-pulse burst of length $\tau_{\rm bur}$ is repeated at the *burst repetition interval* (BRI). The entire echo burst is then processed to obtain a range/Doppler discriminated "snapshot" of the surface, after which the footprint scans to an adjacent location.

With burst pulsing, however, new factors serve to decrease the available dwell time and, consequently, the achievable azimuth resolution. Due to the rapid scanning of the antenna, the azimuthal width of the region imaged by a burst of pulses $x'_{\rm az}$ is given by

$$x'_{\rm az} = x_{\rm az} - \gamma\tau_{\rm bur}. \tag{24}$$

Equation (24) indicates that only the surface region within the usable footprint during the entire burst period can be unambiguously measured. The constraint on allowable values of BRI is given by

$$2\tau_{\rm bur} \le {\rm BRI} \le \frac{x'_{\rm az}}{\gamma}. \tag{25}$$

Here the upper bound on BRI results from the necessity to interleave transmit and receive burst events, and the lower bound results from the requirement to achieve azimuthal continuity of imaged regions on the surface. Inserting the definition of $x'_{\rm az}$ from (24) into (25), we obtain an expression for the maximum burst length, and hence maximum dwell time

$$\tau_d = \tau_{\rm bur} \le \frac{1}{3}\,\frac{x_{\rm az}}{\gamma}. \tag{26}$$

Note that the maximum available dwell time is one third that of the continuous pulsing case, yielding

$$\delta_{\rm az} \ge \frac{12\pi d v_{\rm sc}\sin\theta_{\rm inc} ab}{N_b c}\, f(\theta_{\rm az}). \tag{27}$$

Thus, the timing simplicity obtained with burst pulsing comes at the price of a factor-of-three decrease in achievable azimuth resolution; however, the burst timing used here does not require interleaving of transmit and receive events and thus is freed from the tight constraints imposed by (22) and (23).

Although we have only presented two timing schemes—continuous interleaved pulsing and noninterleaved burst pulsing—hybrid approaches are possible. One option applicable when more than one independent elevation beam is

employed ($N_b > 1$) is to transmit pulse bursts alternately on each beam. In this way, interbeam interference may be avoided. For this case, the reception of the individual pulses within the burst may be interleaved with the transmit events in order to achieve longer integration times than if the scheme illustrated in Fig. 7(b) were strictly adhered to. This timing approach is applied to the L-band design example in Section IV.

F. Scatterometer Measurement Variance

Along with an analysis of spatial resolution, it is essential to consider the issue of backscatter measurement accuracy. The larger the uncertainty in the measured backscatter, the greater the error in the estimate of the desired geophysical parameter. Measurements of radar backscatter cross section are inherently random due to fading effects [7], [29]. A single resolution cell of dimensions $\delta_{\rm el} \times \delta_{\rm az}$ represents one independent "look" at the surface. In order to lower the measurement variance, it is necessary to average multiple independent looks together. In addition to the randomness produced by radar fading, thermal noise in the receiver also contributes to the overall measurement variance. Here, the system tradeoffs associated with minimizing backscatter measurement variance are summarized.

In the presence of thermal noise, an estimate of normalized backscatter cross section (σ^o) is given by

$$\widetilde{\sigma^o} = \widetilde{\sigma^o_{\rm sn}} - \widetilde{\sigma^o_{\rm ne}} \tag{28}$$

where $\sigma^o_{\rm sn}$ is the apparent value of σ^o due to the combined echo signal and noise; $\sigma^o_{\rm ne}$ is the noise-equivalent value of σ^o (i.e., the apparent σ^o if no echo is present and only the thermal noise is processed); and the tilde indicates that the value is an estimate of a random quantity. An estimate of $\sigma^o_{\rm ne}$ is obtained by making an independent measurement of the receiver noise floor in a frequency band separate from the echo band, or at a quiescent time when the echo is not present. This estimate of the "noise-only" component must be subtracted to ensure that estimates of σ^o are not biased high at low SNRs. The noise subtraction process described by (28) is equivalent to that routinely performed in real-aperture pencil-beam scatterometry [29].

As discussed in [29], it is usually possible to obtain a relatively low variance estimate of the noise-only contribution. When this is the case, the normalized standard deviation of the σ^o estimate K_p can be approximated as [5]

$$K_p = \frac{\sqrt{\mathrm{Var}[\widetilde{\sigma^o}]}}{\sigma^o} = \frac{1}{\sqrt{N_{\rm el}N_{\rm az}}}\left(1 + \frac{2}{\rm SNR} + \frac{1}{\rm SNR^2}\right)^{1/2} \tag{29}$$

where $N_{\rm el}$ and $N_{\rm az}$ are the equivalent number of elevation and azimuth looks that are averaged to form the multilook cell, and SNR is the signal-to-noise ratio given by $\sigma^o/\sigma^o_{\rm ne}$. Note that the formation of multilook cells degrades the overall elevation and azimuth resolution to $N_{\rm el}\delta_{\rm el}$ and $N_{\rm az}\delta_{\rm az}$, respectively. In performing system analysis, a convenient approximation to the $\sigma^o_{\rm ne}$ is given by

$$\sigma^o_{\rm ne} = \frac{(4\pi)^3 R^4 L N_0}{P_t G^2 \delta_{\rm el}\delta_{\rm az}\lambda^2 (n_p T_p)} \tag{30}$$

where P_t is the peak transmit power; G is the antenna gain in the direction of the resolution cell; $\delta_{\rm el}$ and $\delta_{\rm az}$ are the dimensions of the single-look resolution cell; R is the slant range to the cell; L is the total system/path loss (including $L_{\rm scan}$); N_0 is the thermal noise power spectral density; T_p is the length of an individual transmit pulse; and n_p is the number of coherently integrated pulses processed to form the cell.

Equations (29) and (30) indicate a key tradeoff that must be performed in the design of high-resolution scatterometer systems. In order to minimize the measurement variance, it is generally desirable to average as many independent looks as possible. As discussed in Section III-D, the ability to achieve fine azimuth resolution given the conically scanning geometry is somewhat limited. Consequently, the ability to average multiple azimuth looks without significantly degrading the ultimate resolution is limited. There is considerably more flexibility to achieve finer elevation resolution, and hence more elevation looks, by utilizing a higher bandwidth transmit signal [see (18)]. As the elevation resolution decreases, however, there is a commensurate decrease in SNR via (30), which tends to increase the measurement variance as expressed in (29). The key tradeoff here, as with other scatterometer systems, is to obtain as many elevation looks as possible without overly degrading SNR.

Another source for additional looks is the overlap in the measurements due to successive rotations of the antenna. The along-track continuity constraint of (13) ensures that measurements along the nadir track are just contiguous, but there may be significant overlap in the measurements in regions of the swath away from nadir. When overlapping resolution cells from successive scans are combined, the total number of looks can be increased without degrading the final resolution associated with the multilook cell.

G. Data Processing Issues

The primary goal of this paper is to address the instrument requirements and theoretical performance of a conically scanning radar employing combined range/Doppler discrimination. It is clear, however, that the addition of Doppler discrimination imposes new requirements on overall data rate and data processing beyond what is needed for current real-aperture pencil-beam systems; however, a treatment of the specific processing algorithms necessary to form the final high-resolution backscatter product is beyond the scope of the present analysis. In addition to performing range/Doppler compression on the raw data, these algorithms must also geolocate the measurements, perform multilook averaging, and, possibly, mosaic measurements from overlapping circular scans of the antenna onto a rectilinear grid. High-resolution radar processing is an expansive and well-studied topic (e.g,. see [5]), and a variety of existing SAR algorithms can be adapted to yield the best solution for the pencil-beam scatterometer case.

One noteworthy indication of processor complexity is the degree to which the Doppler shift of a given scatterer changes over the integration time. Using a criterion similar to that described in [33], we note that when

$$\frac{R\lambda}{2\delta^2_{\rm az}} = \frac{2v^2_{\rm sc}\tau^2_d}{R\lambda} < 1 \tag{31}$$

the Doppler shift change during the dwell time is smaller than the Doppler resolution. When (31) holds, an "unfocused"

TABLE I
EXAMPLE CONICALLY SCANNING SYSTEMS EMPLOYING RANGE/DOPPLER RESOLUTION

Parameter	Example 1: Ku-Band	Example 2: L-Band
Frequency	14 GHz	1.2 GHz
Spacecraft Altitude	800 km	670 km
Measurement Incidence Angle	54°	40°
Antenna Diameter	2.5 m	6.5 m
Antenna Gain	48 dB	36 dB
Number of Elevation Beams	2	2
Rotation Rate	15 rpm	7 rpm
Uncompensated Scanning Loss	-8 dB	-0.1 dB
PRF	7.3 kHz	3.5 kHz
Pulse Length	130 μsec	15 μsec
Burst Timing	τ_d = 1.5 ms, BRI = 3.2 ms	τ_d = 15 ms, BRI = 40 ms
System Loss (compensated for scanning loss)	2 dB	2 dB
N_0	-201 dBW/Hz	-201 dBW/Hz
$\delta_{el} \times \delta az$ ($\theta_{az} = 90°$)	0.07 km × 1 km	0.07 km × 1 km
σ^o_{ne}	-27 dB	-35 dB
K_p ($\sigma^o \gg \sigma^o_{ne}$)	27% (1 dB)	27% (1 dB)

azimuth processing approach may be applied, where the Doppler for each scatterer is essentially assumed constant during the integration time. Because of the relatively short dwell times implied by (20), an unfocused Doppler compression algorithm can often be applied to the pencil-beam scatterometer case, simplifying the processing.

Just as the Doppler shift of a specific scatterer may vary over the integration time, the range may vary as well. This "range walk" effect is known to be potentially severe for high squint angles [33]. To avoid having to correct for range walk, the following condition must hold:

$$\frac{v_g \tau_d}{\delta_{\rm el}} \ll 1. \tag{32}$$

Equation (32) insures that at high squint angles (i.e., extreme forward- or aft-looking directions) that the range cell only moves a small fraction of the overall range resolution. Like (31), (32) often holds for pencil-beam systems because of the very short integration times allowed by the rapidly moving footprint. When both of these conditions apply, a given scatterer may be assumed to be fixed in both range and Doppler.

IV. INSTRUMENT DESIGN EXAMPLES

The application of combined range/Doppler discrimination techniques to pencil-beam scatterometers is illustrated with two system examples of current interest. In each case, the framework described in Section III is used to establish high-level instrument design parameters and performance.

A. Ku-Band Design Example

First, we consider the example of a Ku-band system operating with the same orbit and measurement geometry of the *SeaWinds* scatterometer (see Table I). Assuming a circular reflector antenna is used, the antenna diameter must be increased from 1 m (current *SeaWinds* design) to approximately 2.5 m in order to satisfy the ambiguity constraints as expressed in (11). The antenna size determines the beamwidth, as well as the footprint dimensions on the surface. These parameters then determine the required PRF via (8), which is 7.5 kHz. If only one elevation beam ($N_b = 1$) is employed, the spin rate must be at least 30 r/min to satisfy the along-track continuity constraint in (13). However, to allow a slower spin rate more comparable to the *SeaWinds* case of 18 r/min, two elevation beams are assumed for this example. Despite being slower, the spin rate combined with the narrow antenna beamwidths still leads a relatively high scanning loss of 8 dB. To compensate for this loss, transmit/receive beam steering must be performed on both elevation beams, complicating the antenna feed design somewhat.

The next major consideration is the pulse timing scheme. Because of the very high PRF required, it is difficult to maintain proper interleaving with a continuous pulsing scheme. A much more robust approach for this system is to employ the burst pulsing approach, with bursts of 1.5-ms duration repeated every 3.2 ms, selected to satisfy the constraint of (26). Utilizing (19), we see that the resulting 1.5-ms dwell time yields an azimuth resolution of 1 km for the side-looking geometry. Because no interleaving of transmit and receive pulses is required for the "nonoverlapping" burst mode implementation, the transmit pulses may be as long as $T_p = 130$ μs when linear chirp modulation is employed. With the squint elongation effect taken into account, a resolution of between 1–3 km may be obtained over 70% of the total measurement swath, with the resolution rapidly degrading to the real-aperture limit near nadir (see Fig. 3). This example demonstrates that an order-of-magnitude improvement over the current *SeaWinds* resolution of 25 km

may be obtained by incorporating the techniques described in this paper. The primary instrument enhancement required to achieve this performance is a larger antenna with a more complex feed system. An increase in antenna size is readily feasible, since spinning reflector antennas with diameters 2 m or greater are planned for radiometer missions in the near future (such as the Advanced Microwave Scanning Radiometer instrument on the current ADEOS-II mission).

As an example SNR calculation, assume that 14 range looks are desired for every 1 km in elevation; then $\delta_{\rm el} = 0.07$ km, and $B_t = 2.6$ MHz. With $N_{\rm el} = 14$ and $N_{\rm az} = 1$ for a 1-km side-looking resolution cell, (29) indicates that the variance for each measurement is approximately 1 dB when $\sigma^o \gg \sigma^o_{\rm ne}$. Evaluating (30) for $P_t = 120$ W (an easily achievable Ku-band transmit power with current technology), $G = 48$ dBi, $T_p = 130$ μs, $L = 1.5$ dB, and $N_0 = -200$ dBW/Hz results in $\sigma^o_{\rm ne} = -27$ dB. This compares favorably to the typical values of Ku-band σ^o observed over land (10 dB) and over the ocean (20 dB).

B. L-Band Example

As a second example, we address an L-band system similar to a combined radar/radiometer instrument proposed in [21] for the measurement of soil moisture. For this concept, a 6-m deployable mesh reflector antenna is used at an orbital altitude of 670 km. As in the Ku-band example, two elevation beams are used to reduce the spin rate and consequently the angular momentum that must be compensated for by the spacecraft attitude control system. Unlike the Ku-band example, however, the scanning loss is only -0.1 dB, a consequence of the wider L-band beamwidths as well as the lower orbit. The low scanning loss allows a single antenna feedhorn to be used for both transmit and receive, significantly simplifying the feed design.

Another beneficial consequence of the frequency and measurement geometry of this example is that a lower PRF (3.5 kHz) is required to perform the high-resolution processing, which allows interleaving of transmit and receive events to be achieved more easily. In this design, bursts of 15 ms are alternately transmitted on the inner and outer beams to avoid interbeam interference. Unlike the Ku-band example, however, transmit and receive bursts overlap, and interleaving must be performed. The resultant maximum pulse length is $T_p = 15$ μs. As in the previous example, the length of these bursts yields an azimuth resolution of 1–3 km over most of the swath. A sample SNR and K_p calculation for this design is shown in Table I. Here $\sigma^o_{\rm ne} = -35$ dB, which compares favorably with the backscatter cross section encountered over land (typically -30 to -10 dB). Again, the major design issue is the antenna size. Deployable mesh antennas larger than 6 m have been utilized for space communications, and the issues associated with spinning such antennas for remote sensing applications have been studied in detail [21].

V. Point-Target Response Analysis

In Section III, Doppler discrimination techniques have been adapted to the scanning pencil-beam scatterometer to yield a set of fundamental design equations and constraints. Although these expressions are sufficient to establish an initial conceptual design, more detailed calculations are required to verify the complex interplay between the Doppler geometry, ambiguities, antenna pattern, and scanning motion. A useful tool to perform this more detailed design analysis is the point-target response function (PTRF). The PTRF quantifies the complete surface response associated with a specific scattering element given the transmit signal and antenna illumination. The PTRF exhibits the effects discussed previously—including azimuth elongation, range/Doppler ambiguities, cell resolution—as well as important considerations not yet addressed—such as range/Doppler sidelobes and radiometric calibration. The "ideal" PTRF for a rotating pencil-beam scatterometer is derived in Appendix A. In Fig. 8, the PTRF is computed for the Ku-band example described in Section IV. Note that the resolution and ambiguity levels are as predicted by the design equations presented in Section III. In Fig. 9, the 3-dB contour for the spatial response is shown for different azimuth angles, and the squint elongation predicted in Section III-A is evident.

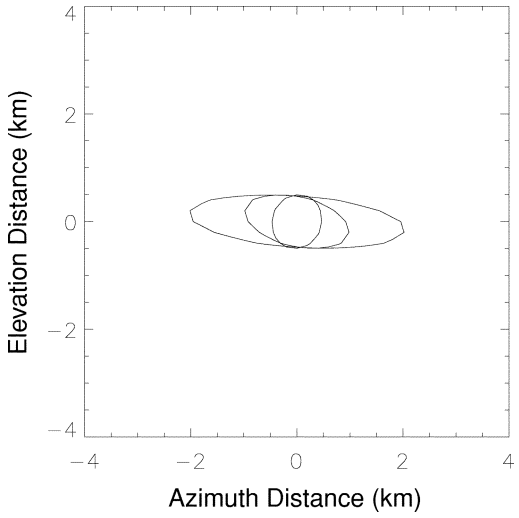

Fig. 9. Comparison of -3-dB contour regions of the example side-looking response function for cross-track distance of 800, 400, and 200 km.

By integrating over the PTRF the effects of sidelobes, shown cascading from the central peak in Fig. 8, can be calculated. When $N_{\rm el}$ is large, the sidelobes in azimuth become the primary issue. If no windowing of the echo return is employed (see the Appendix), the integrated sidelobe ratio (ISLR) is only about -10 dB, which may not be acceptable for many applications. Azimuth sidelobes can be minimized by applying a time-domain window function during processing. When a Hamming window is applied over the dwell period τ_d, the ISLR improves to -16 dB. The windowing, however, degrades the effective azimuth resolution and the measurement variance performance by a factor of approximately 1.6.

VI. Summary and Conclusion

In this paper, we have shown that Doppler discrimination techniques may be employed with pencil-beam systems to achieve significant improvement in spatial resolution over current systems. A set of design equations and an expression for the point target response have been presented to characterize the performance and facilitate design tradeoffs for such a system. Relative to current scatterometer instruments, the main impact of implementing Doppler discrimination is the requirement for

a somewhat larger and more complex antenna. The required antenna diameters are within the range of what is feasible with today's technology and are similar to devices that have flown on other scientific or commercial missions. As briefly noted, processing complexity—either on-board the instrument, within the ground data system, or both—also increases with the necessity to perform Doppler compression. Because resolution on the order of 1 km is obtained the additional processor complexity is modest relative to many conventional SAR systems.

A pencil-beam scatterometer with combined range/Doppler resolution represents a viable alternative to current scatterometer systems. The resolution achieved (order of 1 km) is intermediate between the coarse real-aperture resolution of scatterometers (tens of kilometers) and high-resolution SARs (tens of meters). Further, these measurements are obtained over a very wide swath—providing the frequent revisit time necessary for studying global and mesoscale phenomena—and at near constant incidence angle—often simplifying geophysical parameter retrieval. The utilization of a reflector antenna to form the pencil-beams also allows multiple frequencies, multiple polarizations, and passive radiometer channels to be incorporated more easily than with an array design. These capabilities are becoming important as multichannel techniques are increasingly used to obtain environmental parameters. Thus, with the noted advantages and with no major theoretical or technological barriers, the improved resolution scatterometer approach addressed in this study can be seriously considered for future radar remote sensing missions.

Appendix
Point Target Response Conically Scanning Scatterometer

A powerful tool for evaluating the resolution performance for a particular radar system design and processing approach is the PTRF. It quantifies the processor response at all locations within the scene to a single point scatterer or, equivalently, represents the magnitude-squared response to each location in the target scene when a correlation detector is exactly matched or "tuned" to the range/Doppler characteristics of a particular scatterer. An "ideal" PTRF is achieved when a perfect reference function is employed in the correlation process. Consequently, the PTRF is useful to establish the best theoretical performance of the instrument design if a perfect processor is realized.

Assume a transmit signal of the form

$$p(t)e^{j\phi(t)}e^{j\omega_c t} \tag{A1}$$

where $p(t)$ is the amplitude envelope of the transmitted pulse; $\phi(t)$ is the phase modulation; and ω_c is the transmit carrier frequency.

The echo return from a distributed target can be treated as a collection of returns from many infinitesimal surface patches [29]. Because of the short dwell time associated with a scanning pencil-beam system, each scattering patch is approximated as fixed in range/Doppler space. The echo return from the ith patch is given by a time-delayed, frequency-shifted version of the transmit signal with an additional random phase term

$$\xi_i \sqrt{\sigma_{0,i}} \sqrt{\delta A_i}\, c_i a_i^{\mathrm{tx}}(t) a_i^{\mathrm{rx}}(t) p(t-t_i) e^{j\phi(t-t_i)} e^{j\omega_i t} e^{j\omega_c t} e^{j\psi_i} \tag{A2}$$

where ξ_i is a Rayleigh distributed random variable such that $\mathrm{E}[\xi_i^2] = 1$; $\sigma_{0,i}$ is the normalized backscatter cross section at the patch, δA_i is the area of the patch; t_i is the round-trip flight time of the transmit pulse to the surface patch; ω_i is the Doppler shift of the patch; and ψ_i is a random phase term assumed distributed uniformly over $[0 - 2\pi]$. The terms a_i^{tx} and a_i^{rx} represent the antenna amplitude response in the direction of the patch during transmit and receive respectively. The antenna gains are a function of time because the antenna is rotating during pulse train transmission and reception. The term c_i represents the other system gain terms for the ith patch, defined as

$$c_i^2 = \frac{P_t \lambda^2}{(4\pi)^2 L r_i^2} \tag{A3}$$

where P_t is the transmit pulse power; λ is the radar wavelength; L_i is the atmospheric and system losses; and r_i is the slant range to the patch. The echo return from a collection of infinitesimal patch scatterers can thus be written

$$R(t) = \sum_{i \in \mathcal{F}} \xi_i \sqrt{\sigma_{0,i}} \sqrt{\delta A_i}\, c_i a_i^{\mathrm{tx}}(t) a_i^{\mathrm{rx}}(t) p(t-t_i) \cdot e^{j\phi(t-t_i)} e^{j\omega_i t} e^{j\omega t} e^{j\psi_i} \tag{A4}$$

where the summation is performed over all patches in the radar field of view $\mathcal{F}$.

For a correlation detector, the return echo is first multiplied by

$$w(t-t_0)p(t-t_0)e^{-j\phi(t-t_0)}e^{-j\omega_0 t}e^{-j\omega t} \tag{A5}$$

where t_0 and ω_0 are the time delay and Doppler frequency at the position of the selected scatterer to be detected, and $w(t)$ is a windowing function inserted to reduce sidelobes. Integrating, and then taking the magnitude, the detected signal energy E is

$$E = \left| \int_{-\infty}^{\infty} dt \sum_{i \in \mathcal{F}} \xi_i \sqrt{\sigma_{0,i}} \sqrt{\delta A_i}\, c_i w(t) p(t-t_i) p(t-t_0) \cdot e^{j(\phi(t-t_i)-\phi(t-t_0))} e^{j(\omega_i-\omega_0)t} e^{j\psi_i} \right|^2. \tag{A6}$$

Applying the expectation operator $\mathcal{E}$ to (A6) and assuming that the scattering patches are uncorrelated, we have

$$\mathcal{E}[E] = \sum_{i \in \mathcal{F}} \sigma_{0,i} \delta A_i c_i^2 \cdot \left| \int_{-\infty}^{\infty} dt a_i^{\mathrm{tx}}(t) a_i^{\mathrm{rx}}(t) w(t) p(t-t_i) p(t-t_0) \cdot e^{j(\phi(t-t_i)-\phi(t-t_0))} e^{j(\omega_i-\omega_0)t} \right|^2. \tag{A7}$$

From (A7), the contribution per unit of surface area at the location of the ith scattering patch ζ_i is

$$\zeta_i = c_i^2 \left| \int_{-\infty}^{\infty} dt w(t) a_i^{\mathrm{tx}}(t) a_i^{\mathrm{rx}}(t) p(t-t_i) p(t-t_0) \cdot e^{j(\phi(t-t_i)-\phi(t-t_0))} e^{j(\omega_i-\omega_0)t} \right|^2. \tag{A8}$$

The function ζ can equivalently be expressed as $\zeta(az, el)$, where az and el represent the position of the ith patch in azimuth/elevation space. This function ζ is equivalent to the

response of the system to a point target located at the desired location in delay/Doppler space. As with the closely related radar ambiguity function, the PTRF can be used to simultaneously investigate spatial resolution, ambiguities, and sidelobes.

ACKNOWLEDGMENT

The helpful discussions with B. D. Pollard (Jet Propulsion Laboratory) are greatly appreciated.

REFERENCES

[1] R. Atlas, S. C. Bloom, R. N. Hoffman, E. Brin, J. Ardizzone, J. Terry, D. Bungato, and J. C. Jusem, "Geophysical validation of NSCAT winds using atmospheric data and analyses," *J. Geophy. Res.*, vol. 104, no. C5, pp. 11 405–11 424, May 1999.

[2] E. P. W. Attema, "The active microwave instrument on-board the ERS-1 satellite," *Proc. IEEE*, vol. 79, pp. 791–799, June 1991.

[3] F. Carsey, "Review and status of remote sensing of sea ice," *IEEE J. Oceanic Eng.*, vol. 14, pp. 127–137, Apr. 1989.

[4] D. Chen, M. A. Cane, and S. E. Zebiak, "The impact of NSCAT winds on predicting the 1997/1998 El Nino: A case study with the Lamont–Doherty Earth Observatory model," *J. Geophy. Res.*, vol. 104, no. C5, pp. 11 321–11 327, May 1999.

[5] J. C. Curlander and R. N. McDonough, *Synthetic Aperture Radar: Systems and Signal Processing*. New York: Wiley, 1991.

[6] D. S. Early and D. G. Long, "Image reconstruction and enhanced resolution imaging from irregular samples," *IEEE Trans. Geosci. Remote Sensing*, vol. 39, pp. 291–302, Feb. 2001.

[7] R. Fisher, "Standard deviation of scatterometer measurements from space," *IEEE Trans. Geosci. Electron.*, vol. GE-10, no. 2, Apr. 1972.

[8] A. Freeman, W. T. K. Johnson, B. Honeycutt, R. Jordan, S. Hensley, P. Siqueria, and J. Curlander, "The myth of the minimum SAR antenna area constraint," *IEEE Trans. Geosci. Remote Sensing*, vol. 38, pp. 320–324, Jan. 2000.

[9] K. S. Friedman and X. Li, "Monitoring hurricanes over the ocean with wide-swath SAR," *Johns Hopkins APL Tech. Dig.*, vol. 21, no. 1, pp. 49–57, Jan.–Mar. 2000.

[10] M. H. Freilich, D. G. Long, and M. W. Spencer, "SeaWinds: A scanning scatterometer for ADEOS II—Science overview," in *Proc. IGARSS*, Pasadena, CA, Aug. 8–12, 1994, pp. 960–963.

[11] P. L. Frison and E. Mougin, "Monitoring global vegetation dynamics with ERS-1 wind scatterometer data," *Int. J. Remote Sens.*, vol. 17, no. 16, pp. 3201–3218, 1996.

[12] L. Isaksen and A. Stoffelen, "ERS scatterometer wind data impact on ECMWF's tropical cyclone forecasts," *IEEE Trans. Geosci. Remote Sensing*, vol. 38, pp. 1885–1892, July 2000.

[13] J. A. Johannessen, "Emerging scatterometer applications: Snow and ice session summary," in *Proc. SA Workshop on Emerging Scatterometer Applications*, Noordwijk, The Netherlands, Oct. 5–7, 1998.

[14] J. Kerkmann and D. Klaes, "Perspectives for ASCAT," in *Proc. ESA Workshop on Emerging Scatterometer Applications*, Noordwijk, The Netherlands, Oct. 5–7, 1998.

[15] D. G. Long, P. J. Hardin, and P. T. Whiting, "Resolution enhancement of spaceborne scatterometer data," *IEEE Trans. Geosci. Remote Sensing*, vol. 31, pp. 700–715, May 1993.

[16] D. G. Long and P. Hardin, "Vegetation studies of the Amazon basin using enhanced resolution Seasat scatterometer data," *IEEE Trans. Geosci. Remote Sensing*, vol. 32, pp. 449–460, Mar. 1994.

[17] D. G. Long and M. R. Drinkwater, "Cryosphere studies using NSCAT data," *IEEE Trans. Geosci. Remote Sensing*, vol. 37, pp. 1671–1684, May 1999.

[18] R. K. Moore, "Effect of pointing errors and range on performance of dual-pencil-beam scatterometers," *IEEE Trans. Geosci. Remote Sensing*, vol. GE-23, pp. 901–905, Nov. 1985.

[19] F. Naderi, M. H. Freilich, and D. G. Long, "Spaceborne radar measurement of wind velocity over the ocean—An overview of the NSCAT scatterometer system," *Proc. IEEE*, vol. 79, pp. 850–866, June 1991.

[20] S. V. Nghiem and W.-Y. Tsai, "Using a spaceborne Ku-band scatterometer for global snow cover monitoring," in *Proc. IGARSS*, Hamburg, Germany, June 28–July 2 1998.

[21] E. Njoku, Y. Kim, M. Spencer, W. Tsai, W. Wilson, S. Yueh, J. VanZyl, Y. Rahmat-Samii, and M. Thomson, "A spaceborne L-band radiometer-radar concept for land and ocean surface monitoring," in *Proc. IEEE Aerospace Conf.*, Big Sky, MT, Mar. 10–17, 2000.

[22] J. L. Alvarez Perez, S. J. Marshall, C. Schmullius, M. Habermeyer, and K. Gregson, "Resolution enhancement of ERS scatterometer data," in *Proc. ESA Workshop on Emerging Scatterometer Applications*, Noordwijk, The Netherlands, Oct. 5–7, 1998.

[23] W. G. Pichel and P. Clemente-Colon, "NOAA coastwatch SAR applications and demonstration," *Johns Hopkins APL Tech. Dig.*, vol. 21, no. 1, pp. 49–57, Jan.–Mar. 2000.

[24] Q. P. Remund and D. G. Long, "Sea ice extent mapping using Ku-band scatterometer data," *J. Geophys. Res.*, vol. 104, no. C5, pp. 11515–11 527, May 15, 1999.

[25] Q. P. Remund, D. G. Long, and M. R. Drinkwater, "An iterative approach to multisensor sea ice classification," *IEEE Trans. Geosci. Remote Sensing*, vol. 38, pp. 1843–1856, July 2000.

[26] S. W. Running, J. B. Way, K. C. McDonald, J. S. Kimball, S. Frolking, A. R. Keyser, and R. Zimmerman, "Radar remote sensing proposed for monitoring freeze-thaw transitions in Boreal regions," *EOS, Trans. Amer. Geophys. Union*, vol. 80, no. 19, pp. 213, 220–221, May 11, 1999.

[27] C. C. Schmullius, "Monitoring Siberian forests and agriculture with the ERS-1 wind scatterometer," *IEEE Trans. Geosci. Remote Sensing*, vol. 35, pp. 1363–1366, Sept. 1997.

[28] M. W. Spencer, C. Wu, and D. G. Long, "Tradeoffs in the design of a spaceborne scanning pencil beam scatterometer: Application to SeaWinds," *IEEE Trans. Geosci. Remote Sensing*, vol. 35, pp. 115–126, Jan. 1997.

[29] M. W. Spencer, C. Wu, and D. G. Long, "Improved resolution backscatter measurements with the *SeaWinds* pencil-beam scatterometer," *IEEE Trans. Geosci. Remote Sensing*, vol. 38, pp. 89–104, Jan. 2000.

[30] M. W. Spencer, J. N. Huddleston, and B. W. Stiles, "Advanced design concepts for a SeaWinds scatterometer follow-on mission," in *Proc. IEEE Aerospace Conf.*, Big Sky, MT, Mar. 10–16, 2001.

[31] J. R. G. Townshend, C. O. Justice, D. Skole, J.-P. Malingreau, J. Cihlar, P. M. Teillet, F. Sadowski, and S. Ruttenberg, "The 1-km AVHRR global data set: Needs of the International Geosphere Biosphere program," *Int. J. Remote Sens.*, vol. 15, no. 17, pp. 3417–3441.

[32] W. Y. Tsai, S. V. Nghiem, J. N. Huddleston, M. W. Spencer, B. W. Stiles, and R. D. West, "Polarimetric scatterometry: A promising technique for improving ocean surface wind measurements from space," *IEEE Trans. Geosci. Remote Sensing*, vol. 38, pp. 1903–1921, July 2000.

[33] F. T. Ulaby, R. K. Moore, and A. K. Fung, *Microwave Remote Sensing—Active and Passive*. Reading, MA: Addison-Wesley, 1981, vol. 2.

[34] W. Wagner, "A comparison of ERS scatterometer retrieved soil moisture data with field observations in the Ukraine," in *Proc. ESA Workshop on Emerging Scatterometer Applications*, Noordwijk, The Netherlands, Oct. 5–7, 1998.

[35] V. R. Wismann and K. Boehnke, "Monitoring snow properties on Greenland with ERS scatterometer and SAR," in *Proc. 3rd ERS Symp.*, vol. 2, May 1997, ESA SP-414, pp. 857–86.

[36] V. R. Wismann, "Land surface monitoring with spaceborne scatterometers," in *Proc. ESA Workshop on Emerging Scatterometer Applications*, Noordwijk, The Netherlands, Oct. 5–7, 1998.

Michael W. Spencer received the B.S. degree in physics from the College of William and Mary, Williamsburg, VA, in 1985, and the M.S. degree in planetary science from the California Institute of Technology, Pasadena, in 1987. Through employer-sponsored programs, he received the M.S. degree in electrical engineering from the University of Southern California, Los Angeles, in 1995, and the Ph.D. degree in electrical and computer engineering from Brigham Young University, Provo, UT, in 2001.

From 1987 to 1990, he was with the Aerospace Corporation, Los Angeles, CA, where he was involved in the modeling and analysis of advanced meteorological and surveillance satellite systems. Since 1990, he has been with JPL, where he has worked on the conceptualization, system design, simulation, and calibration of radar remote sensing instruments. His general research interests also include statistical signal processing and data visualization.

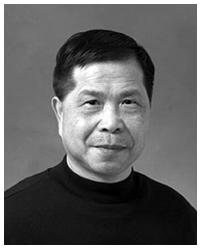

Wu-Yang Tsai received the Ph.D. degree in theoretical physics from Harvard University, Cambridge, MA, in 1971.

He is currently a Principal Engineer at the Jet Propulsion Laboratory, Pasadena, CA, as well as the Project Engineer of SeaWinds on QuikSCAT, SeaWinds on ADEOS-2, and advanced scatterometer projects. He is also the Group Supervisor of the Scatterometer System Engineering Group. He has performed research in high-energy physics, classical and quantum electrodynamics, electromagnetic scattering, propagation and radiation, high-density plasma fusion, high-altitude nuclear explosion phenomenology, radiative heat transfer, synthetic aperture radar, and currently, on all aspects of scatterometer design, algorithm development, and science applications. He coauthored a graduate-level textbook *Classical Electrodynamics* (Reading, MA: Perseus Books, 1998).

David G. Long (S'84–M'89–SM'98) received the Ph.D. degree in electrical engineering from the University of Southern California, Los Angeles, in 1989.

From 1983 to 1990, he was with the Jet Propulsion Laboratory, Pasadena, CA, where he developed advanced radar remote sensing systems. He was Project Engineer in charge of the National Aeronautics and Space Administration (NASA) Scatterometer project, which flew aboard the Japanese Advanced Earth Observing System from 1996 to 1997, and was Experiment Manager for SCANSCAT, the predecessor to SeaWinds. Since 1990, he has been with Brigham Young University (BYU), Provo, UT, where is a Professor of electrical and computer engineering and the Director of the BYU Center for Remote Sensing. He teaches upper division and graduate courses in communications, microwave remote sensing, radar, and signal processing. He is a member of several NASA science teams conducting research in microwave remote sensing, sea ice, and atmospheric dynamics. He has numerous publications in signal processing and radar scatterometry. His research interests include microwave remote sensing, radar theory, space-based sensing, estimation theory, signal processing, and mesoscale atmospheric dynamics.